Philosophical Magazine
2012, 1–20, iFirst

Taylor & Francis
Taylor & Francis Group

Meso-mechanical analysis of deformation characteristics for dynamically triggered slip in a granular medium

M. Griffa[a]*, B. Ferdowsi[a], E.G. Daub[bc], R.A. Guyer[bd], P.A. Johnson[b], C. Marone[ef] and J. Carmeliet[ag]

[a]*Swiss Federal Laboratories for Materials Science and Technology (EMPA), ETH Domain – Überlandstrasse 129, CH-8600, Dübendorf, Zürich, Switzerland;* [b]*Solid Earth Geophysics Group, Los Alamos National Laboratory, MS D443, NM 87545, Los Alamos, USA;* [c]*Centre for Nonlinear Studies, Los Alamos National Laboratory, MS B258, NM 87545, Los Alamos, USA;* [d]*Department of Physics, University of Nevada, Reno (NV), USA;* [e]*Department of Geosciences, Pennsylvania State University, University Park, PA 16802, USA;* [f]*G3 Centre and Energy Institute, Pennsylvania State University, University Park, PA 16802, USA;* [g]*Chair of Building Physics, Swiss Federal Institute of Technology Zürich (ETHZ), Wolfgang-Pauli-Strasse 15, CH-8093, Zürich, Switzerland*

(*Received 26 October 2011; final version received 17 May 2012*)

The deformation characteristics of a sheared granular layer during stick–slip are studied from a meso-mechanical viewpoint, both in the absence and in the presence of externally applied vibration. The ultimate goal is to characterize the physics of dynamic earthquake triggering, where one earthquake, *i.e.*, slip on one fault, is triggered via the seismic waves radiated by another spatially and temporally distant seismic event. Toward this goal, we performed Discrete Element Method simulations of a two-dimensional packing of disks, mimicking a mature geologic fault. These simulations were used to investigate the affine and non-affine deformations inside the granular layer and their spatial–temporal evolution across the stick–slip cycle. The simulation results show that slip in general is accompanied by the appearance of localized regions with high values of both affine and non-affine deformations. These regions are temporally correlated and are mainly concentrated in a shear zone at the interface between the granular layer and the driving block. Dynamic triggering is found to initiate slip when vibration is applied late in the stick–slip cycle, when the system is close to a critical state. It is also found that vibration itself introduces a large amount of affine and non-affine strains, which leads to the initiation of slip at lower shear stress than an equivalent slip event without vibration.

Keywords: granular media; affine and non-affine deformations; dynamic earthquake triggering; stick–slip instability

1. Introduction

The passage of seismic waves radiated by one earthquake source can trigger slip on faults far away from that source [1]. This phenomenon is termed dynamic earthquake

*Corresponding author. Email: michele.griffa@empa.ch

ISSN 1478–6435 print/ISSN 1478–6443 online
© 2012 Taylor & Francis
http://dx.doi.org/10.1080/14786435.2012.700417
http://www.tandfonline.com

Downloaded by [Lib4RI] at 08:15 10 July 2012

triggering [2] and is widespread [3]. It may be that about 50% or more of earthquakes are dynamically triggered by seismic waves [4]. Observations show that triggering earthquakes causes an increase in seismicity rate during a long temporal interval after their occurrence and over distances much larger than the length-scale of the originating fault [5,6].

The physical mechanism responsible for dynamic triggering remains a mystery. It is clear that it may differ significantly from the simplest version of the Coulomb failure model used to explain earthquake nucleation and static triggering (aftershock nucleation) [2,7]. According to this model, an earthquake occurs when tectonic stresses exceed a geologic fault's frictional rock strength. The result is either the formation of a new fault or frictional slip along an existing one. In either case, the critical tectonic stresses have values that are orders of magnitude larger than those of seismic waves radiated by earthquakes far away in space and time. Even though, according to the Coulomb failure model, small dynamic stresses can trigger immediate slip on faults that are already close to failure [8,9], it remains to be explained why a significant part of the dynamic earthquake triggering phenomenology involves delayed triggering, *i.e.*, triggering slip much later in time (days, weeks and even months) compared with the seismic wave passage time [5,10], indicating that other mechanisms, more complex than those described in the simplest version of the Coulomb failure model, are at play [11,12].

To date, insight into the physics of dynamic earthquake triggering has been addressed considering the case of frictional sliding on a fault. Frictional slip leads to (1) the formation of granular fault gouge, due to the wear of the fault's interfacial surfaces, and to (2) cycles of successive earthquakes (slip/stress drops), as a result of steady motion across the fault gouge [7]. It has been hypothesized that granular gouge in mature faults may play a key role in the physical mechanism of dynamic earthquake triggering [8,13]. This hypothesis has been based upon the laboratory scale evidence that mechanical vibrations can change the mechanical behaviour and frictional properties of granular packings, especially of sheared granular layers, in some cases even inducing a transition from a solid-like behaviour to a transient, fluid-like one, that could explain how small dynamic strains could trigger abrupt slip on a fault [14–19].

In the search for validation of the hypothesis about the prominent role of granular friction in dynamic earthquake triggering, Johnson et al. applied transient sound vibration to sheared granular layers and found evidence of triggered slip events [13]. They used a double-direct shear setup developed by Marone et al. [20,21]. This apparatus is capable of manipulating sheared granular layers in a wide spectrum of dynamic regimes, including continuous sliding, intermittent and quasi-periodic stick–slips [15,22,23]. Stick–slip dynamics of laboratory sheared granular layers is a small-scale and simplified version of what happens in a sequence of earthquakes along a fault. A 'slip event' is the equivalent of an earthquake while the following 'stick' period resembles the inter-seismic period of strain energy accumulation [24–26]. Recent results obtained with the double-direct shear setup of Marone et al. and with other ones [27,28] have clearly confirmed the hypothesis that granular layers play a key role in controlling the characteristics of slip events. However, an entire class of questions remains open, *i.e.*, what are the granular mechanics origins of the susceptibility of stick–slipping, sheared layers to be driven into their

Downloaded by [Lib4RI] at 08:15 10 July 2012

pseudo-fluid dynamic phase when an external vibration is applied to their boundaries? Indeed, the behaviour of the granular layer depends upon its microscopic and mesoscopic scale properties. By mesoscopic scale we mean a spatial scale equivalent to the size of clusters made of 10–20 particles. A number of these properties cannot be measured using most of the currently available experimental configurations. On the contrary, numerical simulations of sheared granular layers with Discrete Element Method (DEM)-like approaches allow for characterizing the evolution of the granular dynamics underlying the macroscopic behaviour. Thus they can provide data and information complementary to those obtained in laboratory investigations and they can help with answering the basic questions about the granular mechanics origins of dynamic earthquake triggering.

In a recent study, we proposed a 2D DEM model of a granular layer sheared by deformable, thick blocks mimicking geologic fault rocks. With this model, we investigated the role of AC vibration applied at the boundaries of the deformable blocks in triggering slip events. We performed 2D DEM simulations both with (perturbed simulation runs) and without vibration (reference runs) to explore how vibration affects the particle-scale dynamics of slip [29]. The analysis of the patterns of particle-scale displacements revealed the development of highly localized spatially heterogeneous (non-affine) deformations [30,31].

Deformations (and the respective strain tensor field) inside sheared granular layers can in general be described, at a mesoscopic scale, as consisting of the superposition of two components: a locally uniform strain, called affine, and a residual part associated with highly inhomogeneous and irreversible particle displacements, which we call non-affine. The first type of strain component comes from the usual continuum mechanics description of materials when ignoring their inhomogeneous nature at different scales. According to this description, a material undergoes uniform deformation when subject to uniform loading at the boundaries. The corresponding deformation can be easily described purely by an affine geometrical transformation, resulting from the combination of four other basic geometrical transformations (translation, rotation, shear and scaling). However, since the actual structure of any material is characterized by different levels of inhomogeneities and discontinuities at different scales, even in the presence of uniform boundary conditions the actual deformation is always spatially fluctuating (non-affine), with different degrees of fluctuations at different scales. Our previous investigation suggested that the development of non-affine deformations may be a key process in dynamic triggering of slip events. In this study, we further extend that analysis, looking at not only non-affine deformations but at the overall components of the mesoscopic scale strain field and at its spatial–temporal evolution during stick–slip dynamics, both in the presence and in the absence of externally applied AC vibration.

2. Simulation approach

Each variable in our 2D DEM model is a-dimensional, expressed in terms of the following basic dimensional units: $L_0 = 150\,\mu\text{m}$, $t_0 = 1\,\text{s}$ and $M_0 = 1\,\text{kg}$, for length,

Downloaded by [Lib4RI] at 08:15 10 July 2012

time and mass, respectively. L_0 represents the largest particle radius within the overall model.

The 2D DEM model consists of three main sets of particles, represented in Figure 1a: a top driving block, a mirroring substrate block and a gouge layer. The top driving block is used to confine and shear the simulated granular gouge. This block is modelled as a system of spherical, bonded particles (top of Figure 1a) and is made of two distinct layers. The top layer consists of particles with radius L_0, driven at constant speed $V_{X,0} = 4$ in the shear direction (X). The second layer is thicker and consists of particles with radius distributed within the interval [0.3; 1.0]. Both the uniform and the distributed size particles interact with each other via radial springs [32,33]. This type of spring is formulated as an elastic Hookean spring:

$$F_r = K_r \cdot \Delta r \tag{1}$$

where F_r is the radial force component and Δr is the distance between their centres.

We notice that the choice here of linear elastic springs was motivated by computational simplicity and evidence from previous studies that this type of elastic bond already allows for capturing the most relevant mechanical features of both regular and irregular lattices of bonded particles, including fracture phenomenology [33–36]. In Equation (1), $K_r = 2.9775 \cdot 10^7$ is the radial compressional/tensional spring stiffness. Its value was chosen on the basis of a calibration procedure based upon simulated unconfined compression tests [37]: K_r was adjusted in order to achieve, for the particle assembly, a bulk Young modulus in typical ranges for rock materials [13,38].

A mirroring substrate block (bottom of Figure 1a), constructed similarly to the driving block, represents the second set of particles. Its bottom, a uniform layer of particles with radius L_0, is fixed in X but can be displaced in the Y-direction by a transient AC perturbation.

The driving block and the substrate are elastic models representing both the laboratory and the tectonic shear blocks. They are characterized by two important features.

First, the Particle Size Distribution (PSD) for the second layer of the driving block and the substrate, shown in Figure 1b, introduces surface roughness at the boundary between the shearing blocks and the gouge layer. This roughness contains a variety of spatial wavelengths and is distinct from the roughness obtained with a regular lattice of particles with constant radius. The PSD is the result of the packing algorithm adopted, which exploits a space-filling particle insertion method [37]. Surface roughness is known to be an important ingredient in modelling and simulating granular stick–slip. Laboratory experiments have shown that shear of granular layers made of smooth, spherical particles leads to unstable sliding, including stick–slip dynamics, only in the presence of rough boundary surfaces [23,39]. In addition, there is ample evidence that actual fault rocks are characterized by surface roughness spanning orders of magnitude in dimension [40–43].

The second feature of the driving block and substrate is the elastic deformability, due to the system of bonds among the particles and their geometrical configuration. This feature is important because it allows for dynamic interactions between the

Downloaded by [Lib4RI] at 08:15 10 July 2012

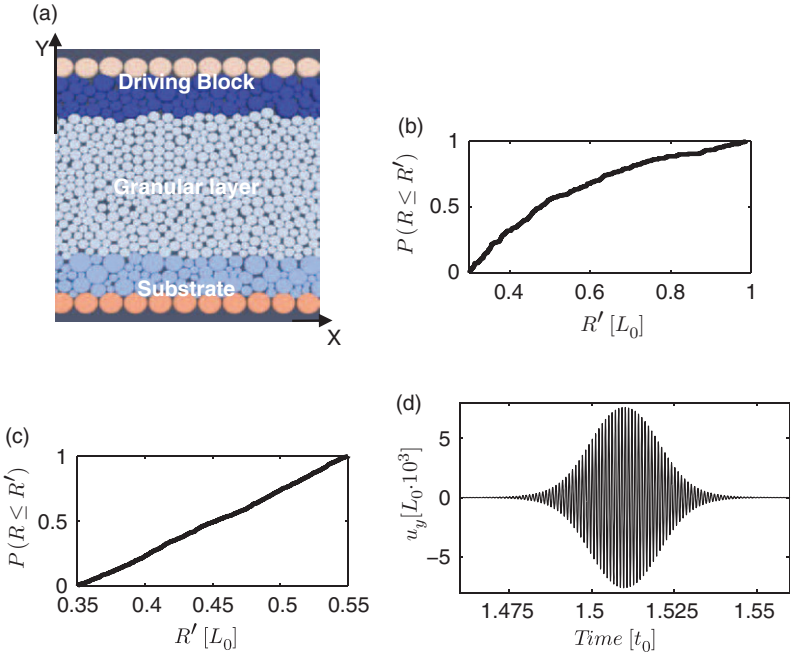

Figure 1. (a) Visualization of a horizontal segment of the 2D DEM model composed of the driving block (top), the granular layer (centre) and the substrate (bottom). Particles are coloured differently in order to identify the different components of the model. A shear load is applied in the X-direction, and a normal confining load is applied in the Y-direction. (b) Cumulative Distribution Function (CDF) of the particle radius R, $P(R \leq R')$, for the particle ensemble comprising the driving block, excluding the top layer particles (those with constant radius L_0). $P(R \leq R')$ represents the probability that the radius R, as a random variable, assumes a value smaller than or equal to R', given the particle ensemble as a realization ensemble for that variable. (c) CDF of the particle radius R, $P(R \leq R')$, for the particle ensemble comprising the granular layer. (d) Example of displacement imposed to the bottom layer of the substrate and in the Y-direction (u_y) as an AC vibration source at the boundary of the system. The temporal law is a harmonic oscillation at frequency $f_0 = 1$ kHz with amplitude modulations given by a Gaussian-like signal. Notice the small peak-to-peak amplitude of this AC displacement, compared to the largest particle size, $L_0 = 150\,\mu$m, within the system, $u_{y,PP} \approx 0.015\ L_0$.

deformed granular gouge and the deformable elastic rocks confining it. These interactions are the basis of earthquake physics. The deformability of the driving block, sliding on top of a rough surface, allows for elastic energy storage/release which is not possible in the case of rigid blocks. Models of spring–slider systems on rough surfaces, such as those belonging to the family of the Burridge–Knopoff model [44,45], usually do not account for the elasticity of the block. Despite its importance, this feature has been included only in a few recently developed DEM models of sheared fault gouge [38,46].

The gouge layer (centre of Figure 1a) consists of a set of spherical, unbonded particles interacting with each other and with the driving block/substrate particles via a repulsive Hookean force with radial and tangential components [32,33].

Downloaded by [Lib4RI] at 08:15 10 July 2012

The radial component has a spring stiffness $K_r = 5.954 \cdot 10^7$. The tangential component represents the frictional force. Its formulation follows the approach proposed by Cundall et al. [47]. The friction parameters are $K_s = 5.954 \cdot 10^7$ and $\mu_s = \mu_d = 0.6$, for the shear spring stiffness and the friction coefficients, respectively. As for the K_r value of the bonded particles belonging either to the driving block or to the substrate, the microscopic parameters of the unbonded particles were chosen on the basis of a calibration aiming at making the granular layer achieve a Young modulus in the same range as the driving block/substrate's.

The granular layer particles are initially arranged using the same type of packing algorithm described above [37], with radius ranging from 0.35 to 0.55, approximately corresponding to the size range, [105; 150] μm, of the silica glass beads used as model fault gouge in the experiments by Johnson et al. (see the 'Methods' section of Ref. [13]). As a result of the packing algorithm and size range used, the PSD for the granular gouge is quasi-uniform in the given range, Figure 1c.

Each particle within the system is subject to a damping force proportional to the particle velocity vector. This viscous force is used to avoid the build up of kinetic energy within the system due to its finite size in the Y-direction.

The overall model has length $L_X = 70$ in X and approximately $L_Y = 30$ in Y. Periodic boundary conditions are applied in X during each simulation, as the aspect ratio used in the laboratory experiments by Johnson et al. [13] is much larger than we can reasonably simulate.

In the Y-direction, the boundary conditions consist of a modified version of the constant normal force/stress boundary condition adopted by Aharonov et al. [48]. A similar implementation was adopted by Capozza et al. in their study of the effects of vibration on granular stick–slip [17].

Each simulation run consists first of a consolidation stage, 10^4 time steps long, when no shear load is imposed. During this initial time interval, the granular layer is compressed, displacing vertically both the top of the driving block and the bottom of the substrate, until the applied normal load reaches a constant value of $\sigma_n = 600$ ($\approx$4 MPa). The chosen value of σ_n was suggested by the experiments of Johnson et al., where the normal confining load was also equal to 4 MPa [13]. This consolidation period results in an initial, transitory regime for the system's thickness in Y, during which it decreases approximately exponentially towards a steady state value. This equilibrium value is achieved well before the end of the consolidation stage. During the shear phase, the normal load is kept constant on the driving block [29]. The shear load is imposed starting at the end of the consolidation stage, initially with a linearly increasing speed until the desired value $V_{X,0}$ is achieved (piecewise linear ramp loading).

For the perturbed runs, *i.e.*, in the presence of applied vibration, the additional boundary conditions consist of imposing a displacement in Y for the bottom, uniform layer of particles belonging to the substrate. These particles were displaced in Y during a finite time interval according to the following temporal law,

$$u_Y(t) = A \cdot \Delta t \cdot \left[\frac{\partial f}{\partial t}(t, t', T_v, \tau) \cdot \cos\left(\omega(t - t') - \frac{\pi}{2}\right) - \omega \cdot f(t, t', T_v, \tau) \cdot \sin\left(\omega(t - t') - \frac{\pi}{2}\right) \right] \quad (2)$$

Downloaded by [Lib4RI] at 08:15 10 July 2012

where

$$f(t, t', T_v, \tau) \equiv \frac{1}{2} \cdot \left[\tanh\left(\frac{t - t'}{\tau}\right) - \tanh\left(\frac{t - (t' + T_v)}{\tau}\right)\right]. \quad (3)$$

In both Equations (2) and (3), $t = m \cdot \Delta t$, $\forall m = 0, 1, \ldots$, is discretized time and Δt is the simulation time step. Equation (2) represents a sinusoid with frequency $\omega = 2\pi \cdot f_0$, with $f_0 = 1$ kHz, whose amplitude is modulated in time by a waveform with a Gaussian-like shape, given by Equation (3). In Equation (2), t' represents a phase shift term for centring the temporal window of AC vibration at different times during the stick–slip dynamics. $\tau = 0.01$ and $T_v = 0.02$, in Equation (3), play respectively the role of a rising/decaying time constant and width for the AC displacement waveform. $A = 0.01$ in Equation (2) is the AC vibration maximum amplitude. Figure 1d shows the AC displacement waveform applied during the time interval [1.46;1.56].

The overall model is implemented using the open source Discrete Element Method code ESyS-Particle, developed at and maintained by the Earth Systems Science Computational Centre of the University of Queensland, Brisbane, Australia. Newton's equations of motion for the centre of mass and for the angle of rotation about the centre of mass of each particle are solved respectively by a first-order, explicit finite difference scheme and by a finite difference rotational leapfrog algorithm [49]. The finite difference time step $\Delta t = 25 \cdot 10^{-6}$ is small enough to guarantee numerical stability and to satisfy the sampling theorem for a vibration signal with maximum frequency $f_{\max} = 2 \cdot 10^5$, which is approximately the maximum sound frequency of vibration in the laboratory experiments by Johnson et al. [13].

Downloaded by [Lib4RI] at 08:15 10 July 2012

3. Affine and non-affine deformations

Different methods have been developed for defining and estimating affine and non-affine strains at a mesoscopic scale, *i.e.*, in the case of granular media, for intermediate-sized clusters of particles. Tordesillas et al. have developed a local measure of non-affine deformation at the scale of each particle and its first ring of neighbours. This measure is based upon a coherent definition of local strain and curvature according to the micropolar theory of continua [50]. The main advantage of this measure is that it naturally accounts for particle-scale rotations and is based upon a local micropolar strain definition whose volumetric average is equal to the corresponding macroscopic strain experienced by the overall assembly.

In this work we adopt a more phenomenological approach that allows us to estimate a local amount of non-affine deformation and to calculate a best fit value for the local affine strain tensor [30]. This measure of non-affine deformation essentially depends only upon particle displacements and not on their single rotations. In this approach, at any simulation time t we consider a small cluster of particles surrounding a given one with position $\boldsymbol{r}_c$ and the displacement of these particles within the time interval $[t;\ t' = t + \delta t]$. We call $\boldsymbol{r}_i$ the relative position of particle i in that cluster at time t, while with $\boldsymbol{r}'_i$ we indicate the respective relative

position at time t'. The positions are relative to the centre of mass of the cluster at the corresponding time [51]. If the overall mechanical deformation of the cluster is completely homogeneous, between time t and t', then each particle i has, at time t', a relative position $\boldsymbol{r}_i'^A$ given by a simple mathematical mapping (geometrical transformation) from its position at time t, *i.e.*, $\boldsymbol{r}_i'^A = \mathbf{E}(t, \delta t, \boldsymbol{r}_c)\boldsymbol{r}_i$, where $\mathbf{E}(t, \delta t, \boldsymbol{r}_c)$ is an affine transformation matrix for the cluster of particles around the one at position $\boldsymbol{r}_c$, at time t. Inside the cluster region and considering only such homogeneous deformation, the relative displacement of each particle, between time t and t', is given by $\boldsymbol{u}_i^A = \boldsymbol{r}_i'^A - \boldsymbol{r}_i = (\mathbf{E}(t, \delta t, \boldsymbol{r}_c) - \mathbf{1}_2)\boldsymbol{r}_i$, where $\mathbf{1}_2$ is the identity matrix of order two. The correspondent deformation matrix, hence the strain tensor, that is obtained by partial derivatives of the components of the displacement vector field, is then independent of the particle position $\boldsymbol{r}_i$, showing how an affine transformation corresponds to a homogeneous strain.

The estimation of $\mathbf{E}(t, \delta t, \boldsymbol{r}_c)$, at each time t and for each particle, with position $\boldsymbol{r}_c$, of a granular medium, can be obtained by formulating an optimization problem, consisting of minimizing the least squares error function $D^2(t, \delta t, \boldsymbol{r}_c) \equiv \sum_{i=1,\ldots,N(\boldsymbol{r}_c)} \left\| \boldsymbol{r}_i' - \boldsymbol{r}_i'^A \right\|^2$, where $N(\boldsymbol{r}_c)$ is the number of particles belonging to the cluster centred in $\boldsymbol{r}_c$. The minimization is done with respect to the elements of $\mathbf{E}$. In 2D, this minimization problem can be solved analytically, as shown in Ref. [30]. Its solution leads to a best fit of the actual, local deformation with an affine transformation model and an estimate of the residual amount of non-affine deformation, given by the corresponding minimum value of $D^2(t, \delta\ t, \boldsymbol{r}_c)$, which we call $D^2_{\min}(t, \delta t, \boldsymbol{r}_c)$. We can thus associate to each particle of the granular assembly, at each time t, an affine transformation matrix, $\mathbf{E}_{\min}$, and a scalar variable $M \equiv \sqrt{D^2_{\min}}$ with the dimension of a length, which represents the local amount of non-affine deformation. We choose the clusters to consist of all the particles whose centres fall within a distance $L = 2.2$ from the reference particle. This number was chosen in order to consider a cluster small enough to provide enough spatial resolution to capture highly localized deformations, but, at the same time, large enough to consider a sufficiently representative number of particles (about 20). The deformation time-scale δt was chosen as $\delta t = 10 \cdot \Delta t$, which is large enough to avoid being dominated by small-scale particle fluctuations, yet small enough to resolve particle motions finer than the overall large-scale flow.

Since the system is not in pure shear mode, each single cluster may rotate around its centre of mass and the affine mapping matrix $\mathbf{E}_{\min}$ is in general not symmetric. Therefore, $\mathbf{E}_{\min}$ is decomposed into a symmetric matrix, $\mathbf{F}$, representing the deformation due to the combination of shear and scaling, and an orthogonal matrix, $\mathbf{R}_\theta$, representing the rotation (in 2D) of the cluster by an angle θ ($\mathbf{E}_{\min} = \mathbf{R}_\theta \cdot \mathbf{F}$). θ is uniquely determined as we restrict $-\pi/2 \le \theta \le \pi/2$. The conventional strain tensor can thus be expressed as $\epsilon \equiv \mathbf{F} - \mathbf{1}_2$. In the analysis presented below, we have adopted the two eigenvalues of ϵ, ϵ_1 and ϵ_2, with $\epsilon_1 \ge \epsilon_2$, and θ as monitoring variables for characterizing the affine component of the deformation process. M is used as a quantitative estimate of the mesoscopic, localized non-affine component. We show in Section 4 detailed spatial–temporal distributions of M, θ, $\delta\epsilon \equiv \epsilon_2 - \epsilon_1$ and $\bar{\epsilon} \equiv (\epsilon_1 + \epsilon_2)/2$, where $\delta\epsilon$ and $\bar{\epsilon}$ correspond to the affine deviatoric and volumetric (eigen)strains, respectively.

Downloaded by [Lib4RI] at 08:15 10 July 2012

4. Results and discussion

4.1. *Spatial distributions of deformations*

In this study, we adopt the friction coefficient, μ_f, as a macroscopic variable identifying the stick–slip dynamics of the granular layer. The friction coefficient is the ratio of the total shear stress on the driving block, τ, to the average normal confining stress, σ_n. This average confining stress is kept constant on the driving block during the simulation, hence an increase in μ_f corresponds to an increase in τ. We refer to periods of increase for μ_f as 'stick' phases, whereas periods of drop of μ_f are called 'slip phases' or simply slip events.

Figure 2a shows the time series of μ_f for the reference run (black line) and for one corresponding perturbed run (grey line). The time interval of AC vibration for this perturbed run, $I = [3.360; 3.460]$, is highlighted by the shaded area in the figure. We notice that while here we report for brevity the results of our analyses for a single stick–slip period from one reference run-perturbed run couple, qualitatively similar results have been obtained when analysing other stick–slip periods from the same couple of runs or from other couples of runs differing from the one used here only for a distinct, random realization of the granular layer (see Appendix A). Figure 2b shows the waveform of the AC displacement imposed at the lower boundary of the substrate. This example shows that the application of AC vibration triggers slip (grey line) sooner in time than in the corresponding case without AC vibration (black line). The drop in μ_f for the dynamically triggered slip (grey line) is smaller than that of the corresponding spontaneous slip (black line). The markers superimposed on the lines in Figure 2a point to times at which the spatial maps of affine strains and non-affine deformation are shown in Figures 3 and 4, for the reference run and the perturbed run, respectively.

Figure 3 contains the spatial map of the non-affine deformation metric, M (first row, insets (a)–(c)), of the affine deviatoric strain, $\delta\epsilon$ (second row, insets (d)–(f)), of the affine volumetric strain, $\bar{\epsilon}$ (third row, insets (g)–(i)), and finally of the affine rotation angle, θ_r (fourth row, insets (j)–(l)). Spatial maps are shown at the three selected time instants during the reference run (different columns, see the corresponding markers in Figure 2a). As can be seen in Figures 3a, d, g and j, at the initiation of slip there is almost no distinguishable deformation. This means that the system is nearly jammed at this moment. Non-affine deformation increases after the initiation of slip. Figure 3b shows the elevated values of non-affine deformation within spatially localized regions at about half of the slip period. This is accompanied by an increase of both the affine eigenstrains and the affine rotation angle almost at the same spatial locations (Figures 3e, h and k). These spatial–temporal patterns suggest the development of a shear zone as described by the Shear Transformation Zone (STZ) theory [52,53].

Affine and non-affine deformations originate at the interface between the granular gouge and the upper roughness layer of the driving block. However, as the system evolves towards the end of the slip event, they develop across almost the whole granular layer. Still, their maximum values are localized along the upper roughness layer throughout the slip period (Figures 3c, f, i and l). Some visible deviation from this pattern is in the affine volumetric strain and the affine rotation

Downloaded by [Lib4RI] at 08:15 10 July 2012

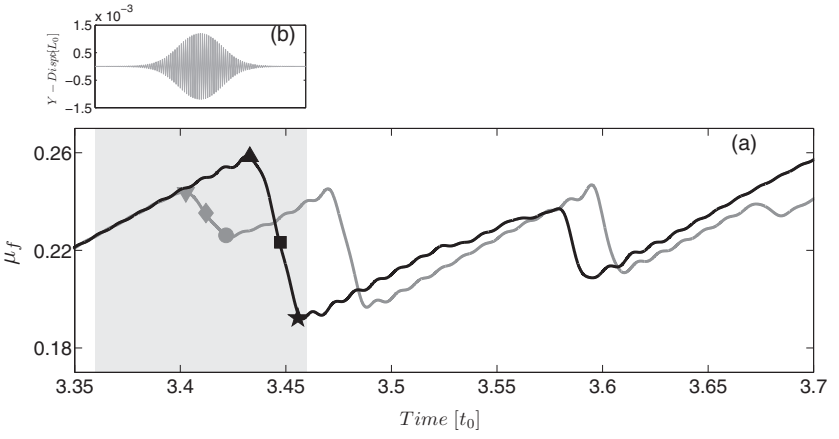

Figure 2. (a) Time series of the friction coefficient, μ_f, for the reference run (black line) and for one perturbed run (grey line). The shaded area indicates the temporal interval of AC vibration ($I = [3.360; 3.460]$). (b) Time history of the substrate's bottom displacement imposed in the Y-direction, u_y, in order to apply vibration to the system. The time axis in this plot has been aligned with the time axis of inset (a) for correspondence. The markers point to time instants and μ_f values for which the spatial distribution of the non-affine deformation metric, M, and of the affine metrics, are shown in Figures 3 and 4, for the reference and perturbed runs, respectively.

Downloaded by [Lib4RI] at 08:15 10 July 2012

angle, whose temporal maximum values appear slightly below the shear zone, at the third time step (Figures 3i and 3l).

Figure 4 shows the spatial maps of the same monitoring non-affine and affine variables but for the perturbed run with AC vibration. Again, different rows refer to different strain metrics while different columns refer to distinct time instants during the corresponding slip period (see the symbols in Figure 2a). In the reference run, both the affine and non-affine deformations are very small at the start of the slip event. However, in the perturbed run, the deformations are much higher from the very beginning of the slip event, Figures 4a, d, g and j. This is a direct consequence of AC vibration and the corresponding elastic wave propagation across the granular layer. Overall deformations of the granular layer are due to the superposition of the deformations caused by the application of shearing and the deformations caused by the imposed AC vibration. Higher levels of affine and non-affine deformations directly imply larger probabilities of particle mobilization. Vibration therefore increases particle mobilization and allows for the initiation and development of slip at reduced shear stress levels.

The passage of the wavefronts due to AC vibration, moving from the lower roughness layer up across the granular layer, is also clearly visible, especially in the spatial map of the affine volumetric strain $\bar{\epsilon}$, Figures 4g, h and i. The volumetric strain is indeed closely related with the compressional (P) elastic wavefield created by the AC vibration displacement applied at the substrate bottom.

Regions of relatively high values (in the present scale) of M, $\delta\epsilon$ and θ_r are no longer only localized at the interface with the upper roughness layer but they are distributed across and along the whole granular layer.

Downloaded by [Lib4RI] at 08:15 10 July 2012

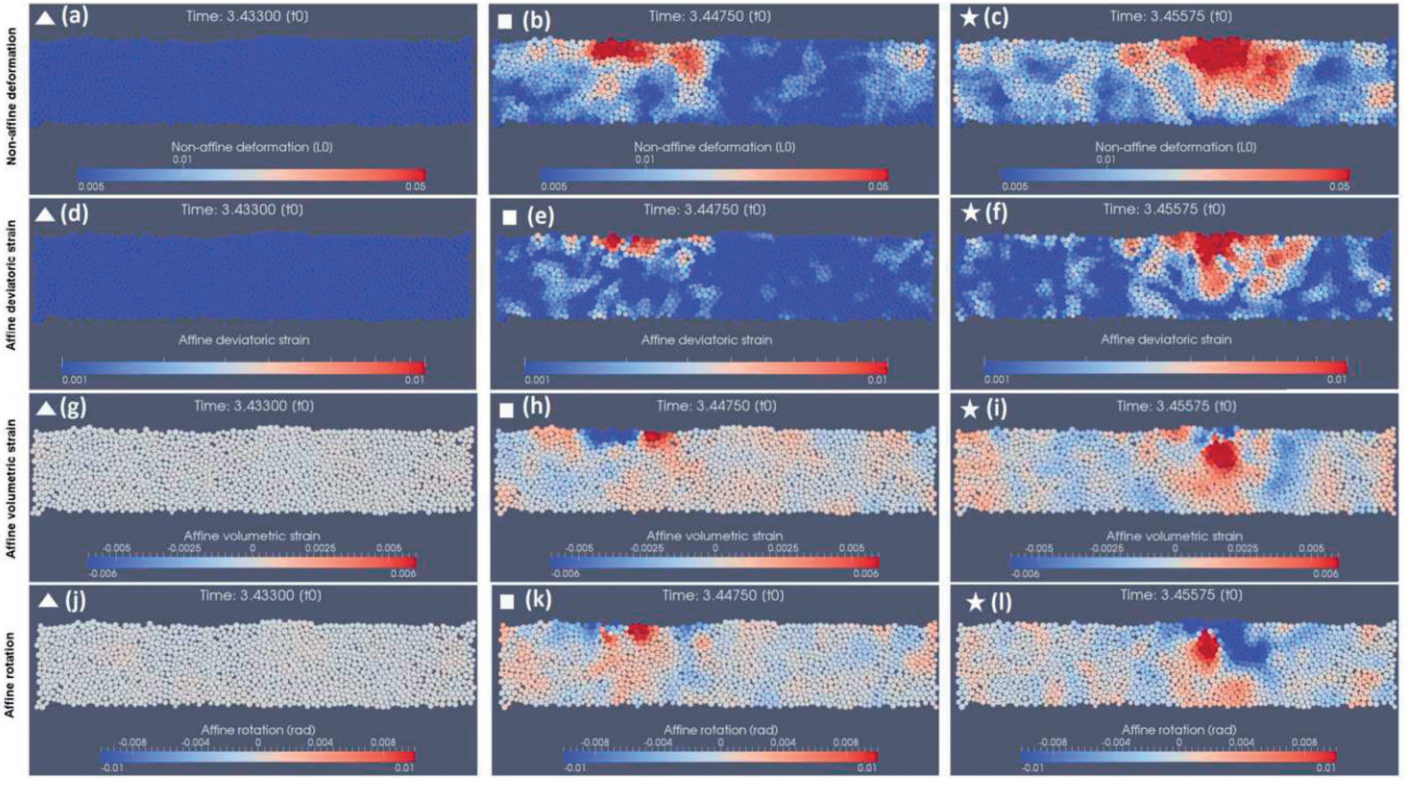

Figure 3. Spatial distribution of the non-affine deformation metric, M (insets (a), (b) and (c)), the affine deviatoric strain, $\delta\epsilon$ (insets (d), (e) and (f)), the affine volumetric strain, $\bar{\epsilon}$ (insets (g), (h) and (i)), and the affine rotation angle, θ_r (insets (j), (k) and (l)), at three different time instants during the reference run slip event, highlighted on the black line in Figure 2a. For M and $\delta\epsilon$, each particle is coloured according to the logarithm of the respective value, while linear colour scales are used for the corresponding spatial snapshots of $\bar{\epsilon}$ and θ_r (note the existence of both negative and positive values for $\bar{\epsilon}$ and θ_r). Complete time series of such snapshots during the stick–slip event are available as animated movies in the online Supplementary Materials.

Downloaded by [Lib4RI] at 08:15 10 July 2012

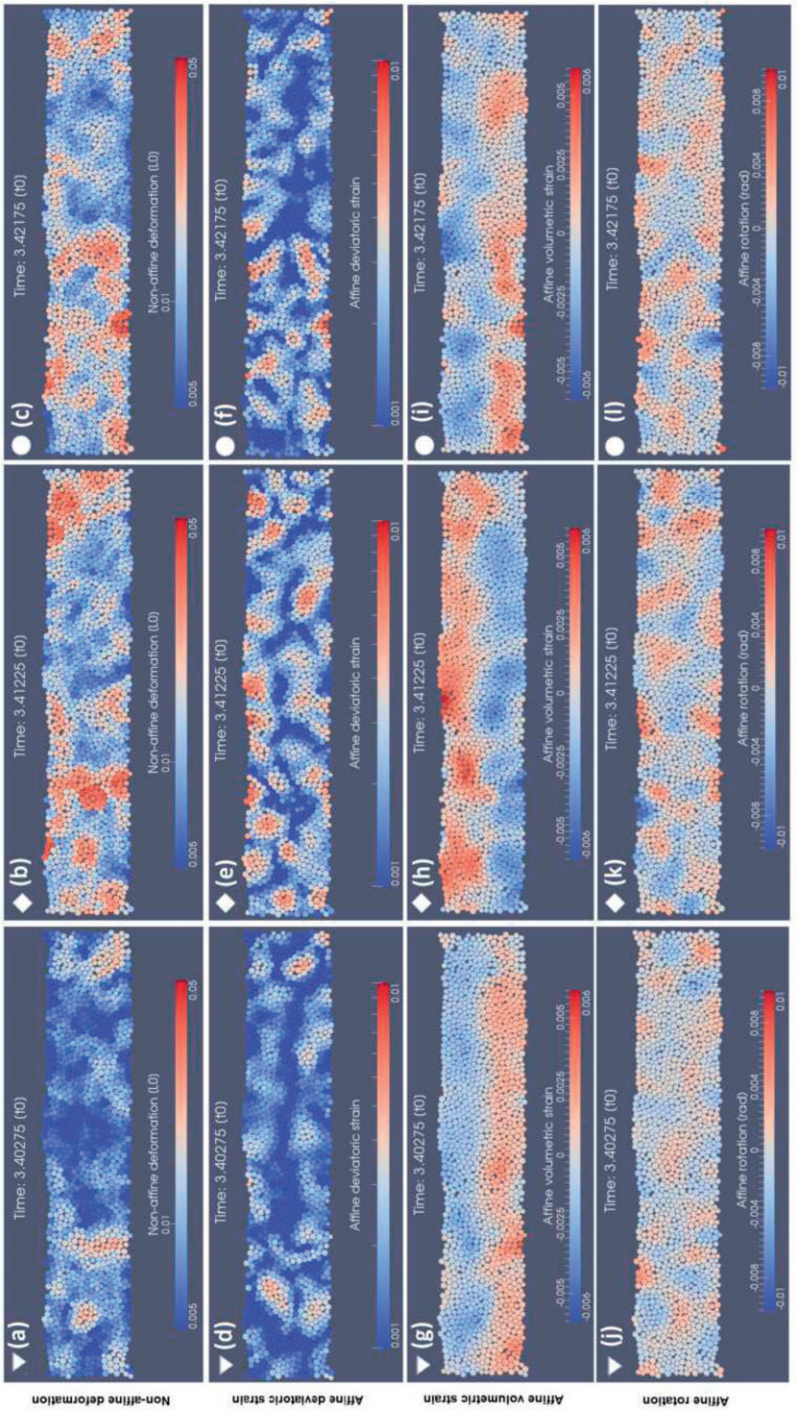

Figure 4. Spatial distribution of the non-affine deformation metric, M (insets (a), (b) and (c)), the affine deviatoric strain, $\delta\epsilon$ (insets (d), (e) and (f)), the affine volumetric strain, $\bar{\epsilon}$ (insets (g), (h) and (i)) and the affine rotation angle, θ_r (insets (j), (k) and (l)), at three different time instants during the slip period of the perturbed run. These snapshots occur throughout the time interval $I = [3.360; 3.460]$ of the application of AC vibration (see Figure 2a, grey line). The corresponding friction coefficient values and locations in time are highlighted by the symbols and correspond to the grey markers in Figure 2a. For M and $\delta\epsilon$, each particle is coloured according to the logarithm of the respective value, while linear colour scales are used for the corresponding spatial snapshots of $\bar{\epsilon}$ and θ_r. Complete time series of such snaphots during the stick–slip event are available as animated movies in the online Supplementary Materials.

4.2. *Temporal evolution of deformations*

In this section we focus on the temporal evolution of the affine and non-affine deformation metrics introduced in Section 3. The particle ensemble averages are used for characterizing the granular layer deformation mode and for comparing it with the state of the system during the stick–slip cycle, quantified by the μ_f signal. Figures 5a and b show time series for several stick–slip cycle signals for the reference and perturbed runs, respectively.

Figures 5a(1) and b(1) show the μ_f signals, highlighting a series of stick–slip events. The ensemble average non-affine deformation metric, $\langle M \rangle$, Figure 5a(2) for the reference run, signals the onset of slip since it abruptly and steeply increases at the start of the drop of μ_f. This abrupt increase happens for each slip event. Figure 5a(2) shows just a short train of spikes in $\langle M \rangle$ but the pattern is exactly the same for a long series of slip events. In general, $\langle M \rangle$ achieves its maximum value at the end of the slip event, after which it slowly decays during the following stick period. Figure 5a(2) indicates that rapid intervals of build-up followed by intervals of slow decay for $\langle M \rangle$ are characteristic patterns of stick–slip dynamics.

The typical temporal evolution of the non-affine deformation is mirrored by the particle ensemble average affine deviatoric strain, $\delta\epsilon$, as can be observed in Figure 5a(3). The cross-covariance of $\langle M \rangle$ and $\langle \delta\epsilon \rangle$ indicates that they are almost completely correlated (see Appendix B for details). This means that the elastic, locally uniform shear deformations develop simultaneously with the irreversible, highly inhomogeneous ones. The fact that both $\langle M \rangle$ and $\langle \delta\epsilon \rangle$ achieve their maximum values simultaneously with the minimum value of μ_f, during the slip period, simply signals the achievement of more degrees of freedom for the particles, corresponding to contact force chain rearrangements.

The particle ensemble average affine volumetric strain, $\langle \bar{\epsilon} \rangle$, Figure 5a(4), is a measure of dilation/compaction. As reported at the beginning of this section, $\langle \bar{\epsilon} \rangle$ strongly correlates with the perturbation due to the elastic wave propagation across the granular layer during the application of AC vibration, which induces compressional waves across the layer. Figure 5a(4) also shows that $\langle \bar{\epsilon} \rangle$ grows at the onset of slip events but it does not exactly follow the same pattern as for $\langle M \rangle$. For instance, larger slip events, in terms of the drop in μ_f, do not necessarily result in higher peak values of $\langle \bar{\epsilon} \rangle$, while this is the case for $\langle M \rangle$ and $\langle \delta\epsilon \rangle$. In addition, $\langle \bar{\epsilon} \rangle$ always fluctuates about 0, assuming both positive and negative values, indicating that the system does not undergo a considerable net elastic volume change. Observed macroscopic dilation and compaction is therefore mainly due to the non-affine (inelastic) deformations.

The particle ensemble average affine rotation angle, $\langle \theta_r \rangle$, is presented in Figure 5a(5). It has a similar trend as for $\langle \bar{\epsilon} \rangle$, building up during slip events and decaying afterwards while always fluctuating about 0. However, we did not find significant correlation between $\langle \theta_r \rangle$ and $\langle \bar{\epsilon} \rangle$.

Results for the same macroscopic signals but related with the perturbed run are presented in Figures 5b(1)–b(5). The shaded area in these plots indicates the time interval of applied AC vibration, $I = [3.36; 3.46]$. As a result of dynamic triggering, the affine and non-affine deformations increase starting earlier in time. The temporal behaviour of the average non-affine and affine deformations $\langle M \rangle$, $\langle \delta\epsilon \rangle$ and $\langle \bar{\epsilon} \rangle$ for the

Downloaded by [Lib4RI] at 08:15 10 July 2012

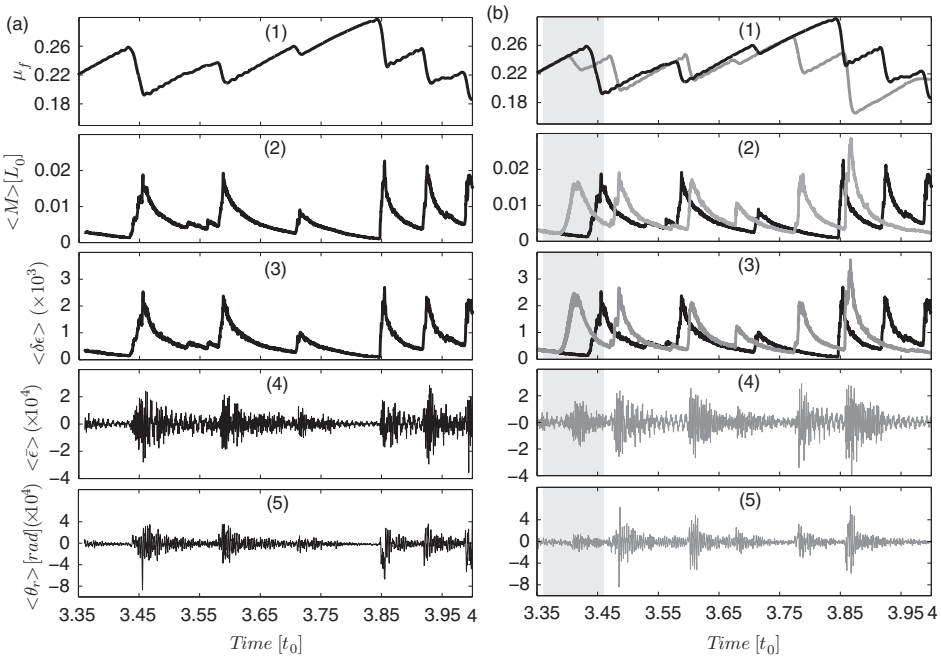

Figure 5. Time series for the reference run (a) and the perturbed run (b): (1) friction coefficient (μ_f), (2) granular layer particle ensemble average of the non-affine deformation metric ($\langle M \rangle$), (3) ensemble average of affine deviatoric strain ($\langle \delta\epsilon \rangle$), (4) ensemble average of affine volumetric strain ($\langle \bar{\epsilon} \rangle$) and finally (5) ensemble average of affine (mesoscopic) rotation angle ($\langle \theta_r \rangle$). Black solid lines refer to the reference run whereas grey lines refer to the perturbed run with $I = [3.360; 3.460]$ as the AC vibration application interval. The shaded area in the perturbed run plots, right column, insets (b), highlight the time interval I.

Downloaded by [Lib4RI] at 08:15 10 July 2012

AC triggered event is quite similar to the reference run, except that the cross-covariance coefficient between $\langle M \rangle$ and $\langle \delta\epsilon \rangle$ is slightly lower during the interval of applied vibration than for the reference run (see Appendix B for details). This is due to the disturbance caused by the elastic wave propagation itself.

5. Conclusions

We have performed 2D Discrete Element Method (DEM) simulations of stick–slip dynamics for a granular layer confined and sheared by thick, elastically deformable blocks. We have run two types of simulations: in the absence (reference run) and in the presence (perturbed run) of AC vibration imposed as a boundary condition at the bottom of the substrate block. The model's basic features are designed to mimic some of the essential features of mature geologic faults containing fault gouge. The AC vibration corresponds to the external perturbation of a fault by seismic waves radiated by earthquakes from other faults in the Earth. Our intent is that this

simulation approach provides the means for investigating the granular dynamics associated with dynamic earthquake triggering, *i.e.*, the nucleation of earthquakes at one fault by the waves emitted by other distant earthquakes. In this work, we have focused on analysing the granular dynamics at a mesoscopic scale, *i.e.*, at the scale of clusters of 10–20 particles.

We have adopted two types of metrics for characterizing mesoscopic scale deformations: the non-affine deformation metric measures the spatial inhomogeneity of the mesoscopic strains, while the affine metrics quantify the spatially homogeneous mesoscopic strains. The mesoscopic scale non-affine deformation analysis of the reference run simulations shows that slip events accomodate shear in zones localized at the interface between the sheared granular layer and the shearing block. This result is in agreement with the Shear Transformation Zone (STZ) theory [52,53] and with the experimental evidence obtained with laboratory configurations employing photoelastic beads [51]. Our analysis of affine deformations indicates that shear localization of non-affine strain is simultaneously accompanied by affine strains which correlate in time, providing more information about the dynamics associated with granular stick–slip.

A critical question that still remains to be answered is which of the two types of deformations contribute most to the stick–slip instability. The temporal analysis we performed in this work just shows that there is a strong correlation between the two types of average deformation signals but cannot underpin any leading role of one deformation mechanism over the other. Correlation of the spatial distribution of affine and non-affine strains will need to be investigated in future work in order to address these open questions.

The affine and non-affine metrics for the perturbed runs show that AC vibration acts as an additional source of both affine and non-affine deformations. The increase in the levels of non-affine deformation, together with the localization of affine strains during stick periods and when AC vibration is applied, could provide an explanation for dynamic triggering: slip requires particle contact mobilization to occur and higher levels of non-affine deformations undoubtedly augment the mobilization likelihood. However, while these metrics provide spatial and temporal information on mesoscopic deformations, we still do not have a clear picture of how slip events initiate.

Beyond assessing the statistical stability of the affine and non-affine deformation patterns when randomly changing the granular layer, we think that important future investigations will have also to address their statistical stability when randomly varying the driving block/substrate and how they are affected by changing their geometrical and mechanical parameters. We believe that one relevant parameter will be the ratio between the thickness of the granular layer and the thickness of the driving block/substrate, given a certain AC vibration frequency and amplitude. The thickness of the driving block/substrate directly affects its elastodynamic features, thus the way the propagated elastic waves interact with the granular layer and perturb the stick–slip dynamics.

Studies of granular stick–slip similar to this study may allow for future work to provide a more quantitative connection between simulation, laboratory, and observational data for earthquakes. DEM simulations provide a unique tool in understanding earthquake dynamics due to access to particle scale deformations, and

Downloaded by [Lib4RI] at 08:15 10 July 2012

allow for analysis similar to our work here to better understand the physics of earthquake initiation at the granular scale. Future work will address other ways to bridge from simulations to observational data, including examining signatures such as the statistical distribution of slip event sizes for real faults (*i.e.*, the Gutenberg–Richter law). Making such connections will provide a more robust way to link simulations, experiments, and observations and allow scientists to gain a better understanding of the physics controlling triggering of slip and failure in the Earth.

Acknowledgments

We would like to thank D. Weatherley and S. Abe for support during the implementation of our DEM model in the ESyS-Particle code and D. Passerone and C. Pignedoli for the help related with the use of the High Performance Computing cluster Ipazia at EMPA. Our work has been supported by the Swiss National Science Foundation (projects No. 206021-128754 and No. 200021-135492) and by the LDRD Program (Institutional Support) at the Los Alamos National Laboratory, Department of Energy, USA.

Downloaded by [Lib4RI] at 08:15 10 July 2012

References

[1] D.R. Shelly, Z. Peng, D.P. Hill and C. Aiken, Nat. Geosci. 4 (2011) p.384.
[2] A.M. Freed, Ann. Rev. Earth Planet. Sci. 33 (2005) p.335.
[3] A.A. Velasco, S. Hernandez, T. Parsons and K. Pankow, Nat. Geosci. 1 (2009) p.375.
[4] D. Marsan and O. Lengline, Science 319 (2008) p.1076.
[5] J. Gomberg, P. Reasenberg, P. Bodin and R. Harris, Nature 411 (2001) p.462.
[6] J. Gomberg, P. Bodin, K. Larson and H. Dragert, Nature 427 (2004) p.621.
[7] C.H. Scholz, *The Mechanics of Earthquakes and Faulting*, 2nd ed., Cambridge University Press, Cambridge, 2002.
[8] P.A. Johnson and X. Jia, Nature 437 (2005) p.871.
[9] D.P. Hill, Bull. Seism. Soc. Amer. 98 (2008) p.66.
[10] D.P. Hill, Science 260 (1993) p.1617.
[11] T. Parsons, Geophys. Res. Lett. 32 (2005) p.L04302.
[12] E.A. Jagla, Europhys. Lett. 93 (2011) p.19001.
[13] P.A. Johnson, H. Savage, M. Knuth, J. Gomberg and C. Marone, Nature 451 (2008) p.57.
[14] S. Luding, E. Clément, A. Blumen, J. Rajchenbach and J. Duran, Phys. Rev. E 49 (1994) p.1634.
[15] H.M. Savage and C. Marone, J. Geophys. Res. 113 (2008) p.1.
[16] A. Janda, D. Maza, A. Garcimartín, J. Lanuza and E. Clément, Europhys. Lett. 87 (2009) p.24002.
[17] R. Capozza, A. Vanossi, A. Vezzani and S. Zapperi, Phys. Rev. Lett. 103 (2009) p.085502.
[18] M.F. Melhus, I. Aranson, D. Volfson and L.S. Tsimring, Phys. Rev. B 80 (2009) p.041305.
[19] M. Pica Ciamarra, E. Lippiello, C. Godano and L. Arcangelisde, Phys. Rev. Lett. 104 (2010) p.238001.
[20] C. Marone, Ann. Rev. Earth. Planet. Sci. 94 (1998) p.17691.
[21] C. Marone, Nature 391 (1998) p.69.
[22] K. Mair and C. Marone, J. Geophys. Res. 104 (1999) p.889.
[23] J.L. Anthony and C. Marone, J. Geophys. Res. 110 (2005) p.1.
[24] W.F. Brace and J.D. Byerlee, Science 153 (1966) p.990.
[25] W.F. Brace and J.D. Byerlee, Science 168 (1970) p.1573.

[26] T. Johnson, F.T. Wu, C.H. Scholz and S. Url, Science 179 (1973) p.278.
[27] K.E. Daniels and N.W. Hayman, J. Geophys. Res. 113 (2008) p.1.
[28] N.W. Hayman, L. Ducloué, K.L. Foco and K.E. Daniels, Pure Appl. Geophys. (2011) p.1.
[29] M. Griffa, E.G. Daub, R.A. Guyer, P.A. Johnson, C. Marone and J. Carmeliet, Europhys. Lett. 96 (2011) p.14001.
[30] M. Falk and J. Langer, Phys. Rev. E 57 (1998) p.7192.
[31] B.A. DiDonna and T.C. Lubensky, Phys. Rev. E 72 (2005) p.066619.
[32] D. Place and P. Mora, J. Comp. Phys. 150 (1999) p.332.
[33] Y. Wang, S. Abe, S. Latham and P. Mora, Pure Appl. Geophys. 163 (2006) p.1769.
[34] Y. Wang and P. Mora, Pure Appl. Geophys. 165 (2008) p.609.
[35] Y. Wang and P. Mora, J. Mech. Phys. Solids 56 (2008) p.3459.
[36] Y. Wang and F. Alonso-Marroquin, Granular Matter 11 (2009) p.331.
[37] M.P.J. Schoepfer, S. Abe, C. Childs and J. Walsh, Int. J. Rock Mech. Min. Sci. 46 (2009) p.250.
[38] K. Mair and S. Abe, Earth Planet. Sci. Lett. 274 (2008) p.72.
[39] K. Mair, K. Frye and C. Marone, J. Geophys. Res. 107 (2002) p.2219.
[40] S. Brown and C.H. Scholz, J. Geophys. Res. 90 (1985) p.12575.
[41] W.L. Power and T. Tullis, J. Geophys. Res. 96 (1991) p.415.
[42] A. Sagy, E. Brodsky and G. Axen, Geology 35 (2007) p.283.
[43] T. Candela, F. Renard, M. Bouchon, A. Brouste, D. Marsan, J. Schmittbuhl and C. Voisin, Pure Appl. Geophys. 166 (2009) p.1817.
[44] R. Burridge and L. Knopoff, Bull. Seism. Soc. Am. 57 (1967) p.341.
[45] J.M. Carlson, J.S. Langer and B.E. Shaw, Rev. Mod. Phys. 66 (1994) p.657.
[46] S. Abe and K. Mair, Geophys. Res. Lett. 32 (2005) p.L05305.
[47] P.A. Cundall and O.D.L. Strack, Geotechnique 29 (1979) p.47.
[48] E. Aharonov and D. Sparks, Phys. Rev. E 60 (1999) p.6890.
[49] Y. Wang, Acta Geotech. 4 (2009) p.117.
[50] A. Tordesillas, M. Muthuswamy and S.D.C. Walsh, J. Eng. Mech. – ASCE 134 (2008) p.1095.
[51] B. Utter and R. Behringer, Phys. Rev. Lett. 100 (2008) p.1.
[52] E.G. Daub and J.M. Carlson, Phys. Rev. E 80 (2009) p.1.
[53] A. Lemaître, Phys. Rev. Lett. 89 (2002) p.4.

Downloaded by [Lib4RI] at 08:15 10 July 2012

Appendix A: Statistical robustness of the affine/non-affine deformation analysis

In order to assess the statistical robustness of the results obtained from the affine/non-affine deformation analysis, we have performed 10 long reference runs, each containing about 900 slip events and each one differing from the others only for a distinct, random realization of the granular layer particle assembly.

Figure A1 shows a temporal segment of the particle esemble average of the non-affine deformation metric, $\langle M \rangle$, for the granular layer, of three such runs. Distinct runs are characterized by qualitatively similar stick–slip dynamics, in terms of both the friction coefficient signal and of the affine/non-affine deformation ones. For brevity, we show here only the non-affine one. The pattern is the same in each simulation. However, the timing for the slip onset is different. From a statistical point of view, the 10 runs exhibit strong agreement with each other. To prove that, we show in Figure A2 the complementary Cumulative Distribution Function (cCDF) for the variable $\Delta\langle M \rangle$. A value of $\Delta\langle M \rangle$ is calculated corresponding to each slip event as the increase in $\langle M \rangle$ corresponding to the onset of slip (see the vertical double arrow in Figure 6 for an example of the value of $\Delta\langle M \rangle$ for one slip event from one reference run). The series of slip events in each run contributes to the generation of an ensemble of realizations for $\Delta\langle M \rangle$, thus treated as a random variable.

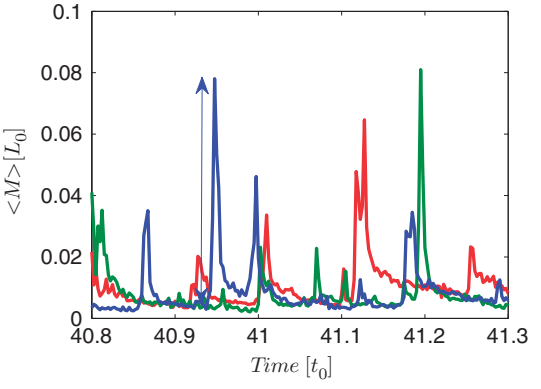

Figure A1. Particle ensemble average of the non-affine deformation metric M for the granular layer, obtained from three different reference runs (different colours). Each run differs from the others only for a different random realization of the granular layer, given the same particle size range. The three runs exhibit different stick–slip signals but with similar qualitative features. The vertical double arrow indicates the increase in $\langle M \rangle$ corresponding to the onset of one slip event, for one of the three reference runs. For each run, we measured such an increase, called $\Delta\langle M \rangle$, corresponding to each slip event.

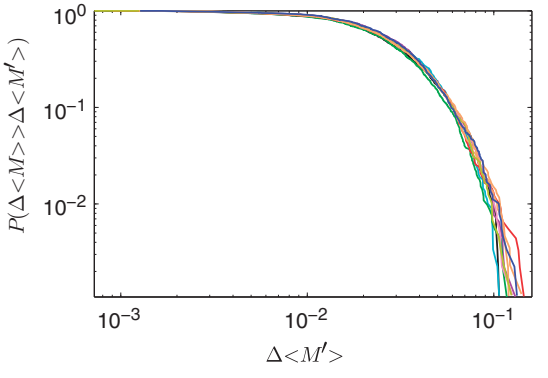

Figure A2. Complementary Cumulative Distribution Function (cCDF) for $\Delta\langle M \rangle$. $P(\Delta\langle M \rangle > \Delta\langle M' \rangle)$ is the probability that $\Delta\langle M \rangle$ achieves a value greater than $\Delta\langle M' \rangle$, given the ensemble of $\Delta\langle M \rangle$ values obtained from the identification of the slip events in a reference run. The different curves (different colours online) correspond to distinct reference runs, each run differing from the others only by a distinct random realization of the granular layer. Ten such reference runs were performed, each one containing approximately 900 slip events.

Figure A2 shows that the fluctuations of $\Delta\langle M \rangle$ due to the random realization of the granular layer are very small, proving that the typical stick–slip pattern described in this article is statistically stable.

Appendix B: Degree of synchronization among affine and non-affine deformations

We investigated the temporal relation between the development of the affine and the non-affine deformation components. Two deformation signals were recorded in vectors

Downloaded by [Lib4RI] at 08:15 10 July 2012

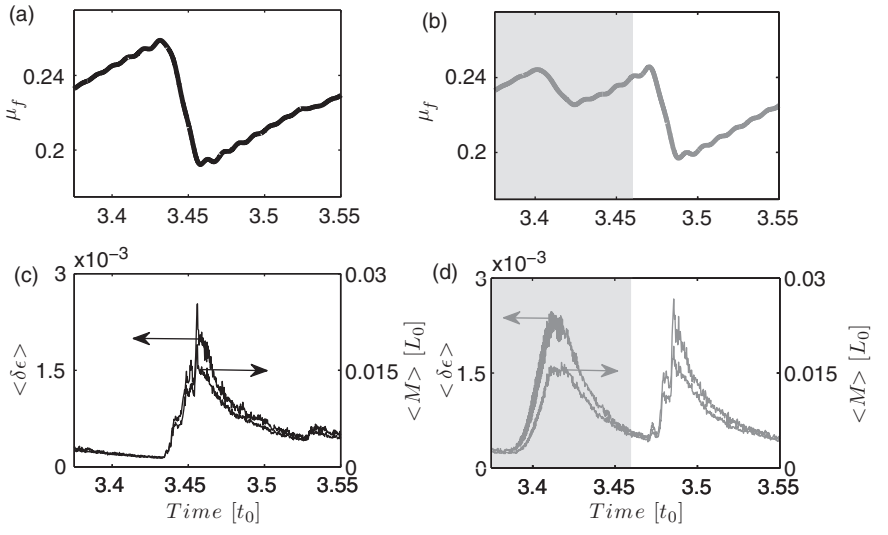

Figure B1. Synchronization among the stick–slip dynamics, the particle ensemble average non-affine deformation metric, $\langle M\rangle$ and the particle ensemble average affine deviatoric strain, $\langle\delta\epsilon\rangle$. Left column (insets (a) and (c)): reference run. Right column (insets (b) and (d): perturbed run with AC vibration applied within the time interval $I=[3.36;3.46]$ (grey shaded area). Top row (insets (a) and (b)): friction coefficient signal. Bottom row (insets (c) and (d)): average affine deviatoric strain (left scale), and average non-affine deformation metric (right scale). $\langle\delta\epsilon\rangle$ and $\langle M\rangle$ are highly synchronized among each other at almost all times and they are strongly correlated to the stick–slip dynamics in terms of the abrupt increase at the onset of slip and slow decay during stick.

$X=(X_1,\ldots,X_n)$ and $Y=(Y_1,\ldots,Y_n)$, respectively. X_i, Y_i, $\forall i=1,\ldots,n$, are the values of the two respective signals at different recording time steps. For measuring the temporal similarity of the two signals we calculated their cross-covariance, defined as:

$$\mathrm{cov}(X,Y)=E\left[\frac{(X-\mu_X)}{\sigma_X}\cdot\frac{(Y-\mu_Y)}{\sigma_Y}\right]. \tag{B1}$$

$E[\cdot]$ is the expected value operator, μ_X and μ_Y are the mean values of X and Y, respectively, and σ_X and σ_Y their respective standard deviations. This cross-covariance definition is such that the corresponding auto-covariance, *i.e.*, the cross-covariance of a signal with itself, at zero time-lag, is equal to 1.0. The cross-covariance function $\mathrm{cov}(X, Y)$ was calculated using different time-lags ΔT between the two signals, with $\Delta\ T=-0.009, -0.0085,\ldots,0.0085, 0.009$. Corresponding to each time-lag value, the two signals were considered only within an evaluation time interval with width equal to two times the average stick–slip event duration, the average value calculated out of a long series of stick–slip events. The evaluation time window's centre was moved along the time axis within the interval [3.4, 4.0] in order to get the temporal evolution of the cross-covariance function itself.

We report here only results about the degree of synchronization between the particle ensemble average of the non-affine deformation, $\langle M\rangle$, and the ensemble average of the affine deviatoric strain, $\langle\delta\epsilon\rangle$. In this case, X represents the time series of $\langle M\rangle$ while Y represents the time series of $\langle\delta\epsilon\rangle$. These two macroscopic signals are strongly correlated with each other and with the stick–slip dynamics as can be seen in Figure B1. Insets (a) and (b) in Figure B1 show stick–slip events, respectively, for the reference run and the perturbed run. The grey shaded area in Figure B1(b) highlights the time period of AC vibration, $I=[3.36;3.46]$, as in Figures 2a and 5b(1)–b(5). Insets (c) and (d) in Figure B1 show the $\langle\delta\epsilon\rangle$ (left scale) and $\langle M\rangle$

Downloaded by [Lib4RI] at 08:15 10 July 2012

(right scale) signals, respectively, for the reference run and the perturbed run. In both runs, $\langle \delta\epsilon \rangle$ and $\langle M \rangle$ are highly synchronized, abruptly increasing corresponding to the slip event till its end, when they achieve local maximum values. During the stick periods, both $\langle \delta\epsilon \rangle$ and $\langle M \rangle$ decrease very slowly, approximately with the same decaying behaviour.

Both in the reference run and in the perturbed run, the zero-lag cross-covariance of $\langle \delta\epsilon \rangle$ and $\langle M \rangle$ is equal to about 0.98 independently of the temporal location of the evaluation window's centre. This result confirms quantitatively the high degree of synchronization between the two signals. The cross-covariance, as a function of time-lag, decreases with different rates corresponding to different evaluation periods, due to the high-frequency fluctuations in the $\langle \delta\epsilon \rangle$ and $\langle M \rangle$ signals themselves. These high-frequency fluctuations make it difficult to estimate a temporal correlation length and compare it across different evaluation periods.

Downloaded by [Lib4RI] at 08:15 10 July 2012